Journal of Solid State Chemistry **152,** 517–525 (1999)
doi:10.1006/jssc.2000.8721, available online at http://www.idealibrary.com on IDEAL®

Neutron Diffraction Study of $La_3Ni_2O_7$: Structural Relationships Among $n = 1$, 2, and 3 Phases $La_{n+1}Ni_nO_{3n+1}$

Christopher D. Ling[1] and Dimitri N. Argyriou

Materials Science Division, Argonne National Laboratory, Argonne, Illinois 60439

and

Guoqing Wu and J. J. Neumeier

Department of Physics, Florida Atlantic University, Boca Raton, Florida 33431

Received January 26, 2000; in revised form March 7, 2000; accepted March 16, 2000

Structural relationships among the $n = 1$, 2, and 3 members of the Ruddlesden–Popper series $La_{n+1}Ni_nO_{3n+1}$ are used to predict a lowering of symmetry in the $n = 2$ phase, subsequently observed and refined against neutron powder diffraction data. Resistivity and magnetic susceptibility measurements are presented for $n = 2$ and 3 that suggest the possibility of a further symmetry lowering at low temperature, such as occurs for $n = 1$; however, no evidence for this is found in low-temperature neutron data. Re-refinement of the $n = 3$ phase reveals significant strain within the perovskite-type layers that appears to increase with n. This strain is used to explain the absence of low temperature phase transformations for $n > 1$. In the absence of a phase transformation, possible origins for the resistivity and susceptibility anomalies are considered.

I. INTRODUCTION

The ternary oxide system La–Ni–O contains a homologous series of layered phases of general composition $(LaO)(LaNiO_3)_n$. These phases are of Ruddlesden–Popper (RP) type, in which n layers of perovskite-type $LaNiO_3$ are separated by single NaCl-type LaO layers. RP phases have been the subject of intense interest in recent years due to their exhibition of properties such as high-T_c superconductivity and colossal magnetoresistance in a variety of systems, particularly those involving mixed-valent cations in the perovskite layer. The average oxidation state of nickel in the system $La_{n+1}Ni_nO_{3n+1}$ ($n = 1$, 2, 3, ∞) varies from 2+ at $n = 1$ to 3+ at $n = \infty$, and as a consequence the series has been investigated for potential magnetic, electronic, and charge-ordering properties.

[1] To whom correspondence should be addressed. E-mail: cling@anl.gov.

Synthesized in air, the $n = 1$ phase has a slight oxygen excess. $La_2NiO_{4+\delta}$, $\delta \approx 0.15$ (1), crystallizes in a tetragonal $F4/mmm$ (a nonstandard setting of $I4/mmm$) structure in which excess oxygen atoms occupy interstitial sites along the stacking axis (2). Reduced to stoichiometry ($\delta = 0$), La_2NiO_4 breaks $F4/mmm$ symmetry below $T_0 \approx 770$ K and adopts an orthorhombic *Bmab* (nonstandard setting of *Cmca*) structure (Fig. 1*a*). The mode by which the structure distorts at T_0 is a rotation of NiO_6 octahedra about (1 0 0). At $T_1 \approx 80$ K, La_2NiO_4 transforms to a tetragonal $P4_2/ncm$ phase in which NiO_6 octahedra are rotated about (1 1 0). The low-temperature transition at T_1 is foreshadowed in the *Bmab* regime by strong anisotropic broadening of reflections indicating orthorhombic strain. Below $T_N \approx 330$ K, La_2NiO_4 is a three-dimensionally antiferromagnetically ordered insulator (1). $La_2NiO_{4+\delta}$ is a semiconductor (3).

Although the $n = 2$ phase $La_3Ni_2O_{7-\delta}$ as synthesized in air is reported to have a slight oxygen deficiency $\delta \approx 0.08$, annealing in high-pressure O_2 gives stoichiometric $La_3Ni_2O_7$, and annealing in H_2 can increase δ as far as 0.65 (4). Structurally, the $n = 2$ phase is of particular interest because the stoichiometric phase $La_3Ni_2O_7$ has an average nickel oxidation state of 2.5, raising the possibility of a charge-ordered Ni^{2+}/Ni^{3+} superstructure. $La_3Ni_2O_7$ is, however, a paramagnetic metal, and its structure is reported as orthorhombic *Fmmm* (with only one Ni site) on the basis of Rietveld-refined X-ray powder diffraction (XRD) data (4). $La_3Ni_2O_{6.92}$ is also reported as *Fmmm*, but semiconducting (4), and therefore possibly weakly charge-ordered. Local charge-ordering models for various values of δ have been proposed to explain a slight anomaly in the resistivity at approximately 120 K (5). The $\delta = 0.35$ phase is tetragonal $I4/mmm$ (4).

0022-4596/00 $35.00

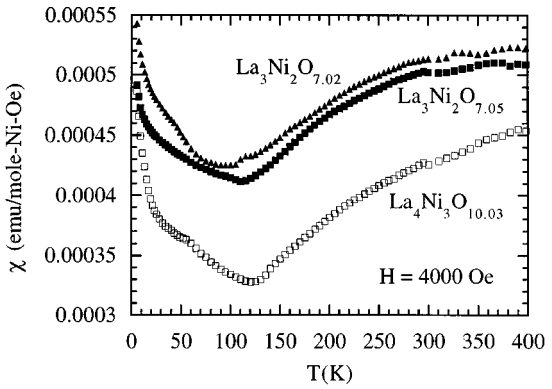

FIG. 1. Magnetic susceptibility χ versus temperature for $La_3Ni_2O_{7.02}$ (filled triangles), $La_3Ni_2O_{7.05}$ (filled squares), and $La_4Ni_3O_{10.03}$ (open squares) in an applied magnetic field of 4000 Oe.

Air-annealed $n = 3$ samples are nearly stoichiometric $La_4Ni_3O_{10}$ (6). Like the $n = 2$ stoichiometric phase, it is a paramagnetic metal, and when reduced becomes a semiconductor (7). The structure is reported on the basis of Rietveld-refined powder neutron diffraction data as orthorhombic *Cmca* (8). This *Cmca* structure is distorted from an *Fmmm* parent structure in the same manner as is La_2NiO_4, i.e., NiO_6 octahedral rotations about *a*. A low-temperature transition equivalent to that occurring at T_1 in the $n = 1$ phase (2) has not been found; however, an anomaly has been observed in the resistivity at approximately 160 K, which may relate to such a transition.

The purpose of this study was a reinvestigation of the $n = 2$ and 3 phases in the system $La_{n+1}Ni_nO_{3n+1}$ using neutron powder diffraction, in order to determine whether low-temperature nuclear and magnetic structural features seen in the $n = 1$ phase are present in the higher-order phases. In the $n = 2$ case, we sought evidence for an equivalent to the *Fmmm–Bmab* transition observed when $n = 1$ and 3. In the $n = 2$ and 3 cases, we sought evidence for an equivalent to the *Bmab–P*4_2*/ncm* transition observed when $n = 1$. We also investigated the possibility of charge-ordering in nonstoichiometric ($\delta \approx 0.08$) $n = 2$.

II. EXPERIMENTAL PROCEDURES

Specimens with compositions $La_3Ni_2O_7$ and $La_4Ni_3O_{10}$ were prepared using two synthesis routes. A 5 g $La_3Ni_2O_{7.02}$ specimen was prepared from high-purity La_2O_3 and NiO starting materials. The oxides were weighed in stoichiometric quantities, mixed in an agate mortar, and reacted at 1075°C overnight followed by a 6 min regrinding and identical overnight reaction. The specimen was reground and reacted at 1100°C overnight; this was repeated five times. The last three regrindings were followed by pressing into pellet form. Finally, the specimen was removed from the furnace and cooled rapidly to room temperature. The resulting specimen has $n = 1$ and $n = 3$ RP phase analogues, as well as NiO, as minor impurity phases (from Rietveld refinements: the $La_3Ni_2O_{7.02}$ sample contained 6.7(3) wt % $n = 3$, 3.42(11) wt % $n = 1$ and 1.80(3) wt % NiO; the $La_3Ni_2O_{7.05}$ sample contained 0.64(3) wt % NiO; and the $La_4Ni_3O_{10.03}$ sample contained 1.08(2) wt % NiO). The 6 g $La_4Ni_3O_{10.03}$ and $La_3Ni_2O_{7.05}$ specimens were made by weighing high-purity La_2O_3 and NiO in stoichiometric quantities and dissolving in 17 ml of HNO_3. This mixture was gently boiled for 20 min, yielding a gray solid that was dried overnight at 450°C. In the case of $La_3Ni_2O_{7.05}$, the specimen was reground for 5 min and reacted at 1125°C for 4 h followed by a 5 min regrinding and reaction for 48 h at 1125°C; this last regrinding and reaction was repeated once. The specimen was then reground for 5 min and reacted at 1150°C for 6 days; this step was repeated once. Finally, the specimen was soaked at 500°C in oxygen for 2 days and slowly cooled to room temperature overnight. In the case of $La_4Ni_3O_{10.03}$, the specimen was reground for 30 min and reacted at 1000°C overnight. Subsequently, the specimen was reground for an average of 10 min and reacted for 1–2 days at 1000°C; this was repeated 12 times before a final regrinding, pressing into pellet form, and reaction at 1000°C. The specimen was cooled quickly to room temperature by removal from the furnace. A previous $La_4Ni_3O_{10}$ specimen reacted at 1060°C contained a significant amount of $La_3Ni_2O_7$. All reactions, unless otherwise stated, were conducted in air.

The average Ni valence was determined by iodometric titration under the assumption that the valences of La and Ni in acidic solution are $+3$ and $+2$, respectively. A carefully weighed amount of sample (about 15 mg) is placed in a test tube from which the air is purged with argon gas; 6 ml of 2 M KI is added. The solution is stirred and 6 ml of 2 M HCl is added and allowed to dissolve the specimen thereby creating I_2 ions as Ni^{3+} is converted to Ni^{2+}. After the addition of a starch indicator, a 0.01 M sodium thiosulfate solution ($Na_2S_2O_3$) was carefully titrated to determine the amount of I_2 and thereby the amount of Ni^{3+} in the specimen. This process was conducted three times for each specimen. All solutions were made with distilled H_2O which was boiled to remove excess CO_2. The stated oxygen concentrations have an uncertainty of ± 0.01. Phase identification through XRD was conducted at various stages of the preparations to monitor the reactions; impurities could not be detected by this method in the final products.

Temperature-dependant time-of-flight (TOF) neutron powder diffraction data were collected for $La_3Ni_2O_{7.02}$, $La_3Ni_2O_{7.05}$, and $La_4Ni_3O_{10.03}$ on the Special Environment Powder Diffractometer (SEPD) at Argonne National Laboratory's Intense Pulsed Neutron Source (IPNS). Higher resolution, room-temperature, TOF neutron powder diffraction data were collected for $La_3Ni_2O_{7.02}$ on the General

Purpose Powder Diffractometer (GPPD) at the same facility. All data were analysed using the program GSAS (9). Electrical resistivity was measured using a four-probe dc method. Magnetic susceptibility measurements were conducted at 4000 Oe using a commercially available SQUID magnetometer.

III. RESULTS

Properties

Magnetic susceptibility measurements conducted at an applied magnetic field $\mathbf{H} = 4000$ Oe are presented in Fig. 1. The specimens were cooled to 5 K at $\mathbf{H} = 0$ prior to the application of field. A weak feature near 50 K evident in two of the curves is due to the presence of adsorbed oxygen, which is difficult to completely eliminate in these weakly magnetic highly porous specimens. The data in Fig. 1 are similar to those reported in previous publications (4–6, 10). The magnitude of the magnetic susceptibility χ per Ni ion at 300 K is comparable to that of metallic $LaSrNiO_4$ (11) and metallic $LaNiO_3$ (12). The large magnitude of χ suggests a Van Vleck contribution associated with the existence of low-spin and high-spin Ni species. The temperature dependence of χ indicates that fully oxygenated $La_3Ni_2O_7$ and $La_4Ni_3O_{10}$ possess few intrinsic localized magnetic moments. Fits to a Curie–Weiss type equation to the low-temperature region below 15 K provide a Curie–Weiss constant of 5 erg-K/mole-Ni-Oe^2 for the three specimens. This translates into an average spin of $S \approx 0.1$ on the nickel site. Both $La_3Ni_2O_7$ and $La_4Ni_3O_{10}$ contain mixtures of Ni^{2+} and Ni^{3+} (1 : 1 in the former case, and 1 : 2 in the latter case). The high-spin state of Ni^{3+} would be $S = \frac{3}{2}$, and the low-spin state, $S = \frac{1}{2}$. In the case of Ni^{2+}, the high-spin state would be $S = 1$ and the low-spin state $S = 0$. It is therefore hard to understand the value of $S \approx 0.1$ observed in the low-temperature region as simply attributable to local non-interacting Ni magnetic moments, even if a low-spin state is assumed for all Ni ions. High-temperature measurements (5) of χ reveal a peak in χ versus T above 400 K in both $La_3Ni_2O_7$ and $La_4Ni_3O_{10}$, which could result from dynamic two-dimensional antiferromagnetic order as displayed in the structurally similar copper oxides (13). If this scenario is correct, the lower magnitude of χ per Ni ion for the $n = 3$ compound suggests that the antiferromagnetic correlations are stronger for the $n = 3$. Another possibility is the existence of a spin gap as observed in the copper oxide ladder compounds (14), which could cause a peak in $\chi(T)$. These possibilities will be evaluated in detail in a future publication (15).

The electrical resistivity ρ for the three specimens is presented in Fig. 2 and reflects behavior similar to that reported earlier (4–6, 10). As shown previously, ρ for $La_3Ni_2O_7$ is sensitive to the oxygen concentration becoming more conductive as the oxygen concentration increases.

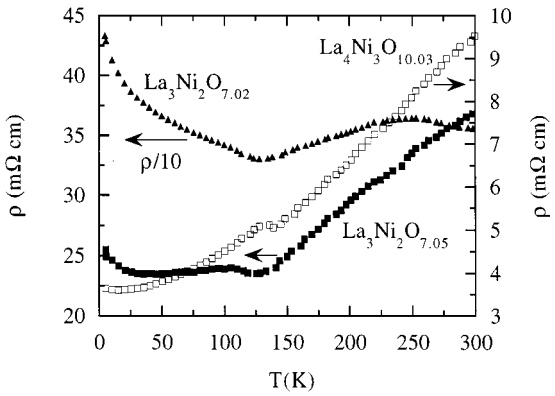

FIG. 2. Electrical resistivity ρ versus temperature for $La_3Ni_2O_{7.02}$ (filled triangles) and $La_3Ni_2O_{7.05}$ (filled squares). The ρ data for $La_3Ni_2O_{7.02}$ are divided by 10, and the left abscissa is used for both $n = 2$ specimens. The ρ data for the $La_4Ni_3O_{10.03}$ specimen (open squares) refer to the right abscissa.

The large variation in the temperature dependence of ρ for fully oxygenated specimens (4–6, 10) indicates that ρ is very sensitive to the oxygen content, and that the resistivity is strongly influenced by grain boundary conductivity in these porous polycrystalline specimens. The feature in the $n = 2$ specimens near 130 K appears in all previous reports, although in the present study it appears to be more pronounced; local charge-ordering models have previously been proposed to explain it (5). The electrical resistivity for the $n = 3$ specimen is more than a factor of 2 smaller than the $n = 2$. A pronounced peak appears at 140 K which is observed in some $La_4Ni_3O_{10}$ specimens (8) and in $Pr_4Ni_3O_{10}$ and $Nd_4Ni_3O_{10}$ (6). A charge density wave has been proposed as the origin of this feature, as have possible temperature-dependent structural changes (6). The resistivity anomalies observed for these $n = 2$ and $n = 3$ samples is considered in the analysis of temperature-dependent neutron powder diffraction data described below.

Structure of $La_3Ni_2O_{7.02}$

The previously reported *Fmmm* structure of $La_3Ni_2O_{7.02}$ (4) provided a reasonably good fit to our room-temperature neutron (GPPD) data; however, a number of weak yet clearly resolved peaks were not indexed by this *Fmmm* model or either of the minor impurities NiO and La_2NiO_4. The most obvious explanation was the presence of an NiO_6 octahedral rotation mode about *a*, as found in the room temperature structures of the $n = 1$ (2) and $n = 3$ (8) RP phases in this system. The resultant space-group symmetry for both $n = 1$ and $n = 3$ is *Cmca*; however, Rodriguez-Carvajal *et al.* (2) chose the nonstandard setting *Bmab* for La_2NiO_4 in order to clarify the relationship to its high- and low-temperature tetragonal forms, by retaining *c* as the long

(stacking) axis. Applying the same rotational mode to the *Fmmm* structure of $La_3Ni_2O_{7.02}$, and similarly retaining *c* as the long axis, gives a resultant space-group symmetry *Amam*, a nonstandard setting of *Cmcm* with allowed reflections at the *d* spacings of the observed peaks unfitted in *Fmmm*.

Applying a small initial rotation of the NiO_6 octahedra and refining the positional and isotropic displacement parameters in *Amam* led to a satisfactory fit to our data. Refined anisotropic displacement parameters on oxygen atom sites were found to be reasonable (Fig. 7*a*). Refining fractional occupancies on oxygen atom sites did not result in statistically significant deviations from 100%, therefore this degree of freedom was removed from the final refinement. No attempt was made to locate interstitial excess oxygen atoms, as for the $n = 1$ phase $La_2NiO_{4+\delta}$ (2), due to the insignificant extent of that excess (0.3% according to the titration results). Impurity phases [NiO, La_2NiO_4 (2), and $La_4Ni_3O_{10}$ (8)] were modeled from previous reports; only unit cell dimensions and phase fractions were refined, in order to minimize possible correlations with refined structural parameters of $La_3Ni_2O_{7.02}$. The final refined structure of $La_3Ni_2O_{7.02}$ is presented in Table 1 and Fig. 3b, and the fit to observed data is shown in Fig. 4.

Rietveld-refinement results using the space groups *Fmmm* and *Amam* are compared in Table 2. Comparison of Ni–O bond distances makes it clear that the NiO_6 octahedral rotation about *a* is rigid (note that O3 in the *Fmmm* setting is split into O3 and O4 in the *Amam* setting). Empirically calculated atomic valences (16) are much improved in *Amam*. The lanthanum atoms in particular are slightly underbonded (with respect to their nominal valence of 3 +) in *Amam* but are much more so in *Fmmm*. This underbonding of lanthanum atoms in *Fmmm* may therefore be the driving force behind symmetry lowering. Note that the composition $La_3Ni_2O_{7.02}$, obtained from iodometric titration, implies an average valence for Ni of 2.52.

TABLE 1
Crystal Structure Data for $La_3Ni_2O_{7.02}$ from GPPD Neutron Powder Data at 300 K

	Amam (*Cmcm*)[a]: $a = 5.39283(11)$, $b = 5.44856(11)$, $c = 20.5185(5)$ Å				
	x (*a*)	*y* (*b*)	*z* (*c*)	$100U_{iso}$ (Å^2)	Valence[b]
La1	$\frac{1}{4}$	0.2534(11)	$\frac{1}{2}$	0.91(7)	2.750
La2	$\frac{1}{4}$	0.2599(6)	0.31886(9)	0.64(5)	2.817
Ni	$\frac{1}{4}$	0.2548(6)	0.09568(9)	0.59(4)	2.562
O1	$\frac{1}{4}$	0.2938(11)	0	0.9(2)	1.841
O2	$\frac{1}{4}$	0.2189(8)	0.2038 (2)	1.76(16)	1.707
O3	0	$\frac{1}{2}$	0.10442(19)	0.70(19)	2.106
O4	$\frac{1}{2}$	0	0.08837(19)	1.2(2)	2.020
	$100U_{11}$ (Å^2)	$100U_{22}$ (Å^2)	$100U_{33}$ (Å^2)	$100U_{12}$ (Å^2)	$100U_{23}$ (Å^2)
O1	0.9(2)	1.5(3)	3.0(3)	0	0
O2	1.76(16)	1.9(2)	1.35(14)	0	−0.2(2)
O3	0.70(19)	0.62(16)	1.8(2)	0.01(13)	0
O4	1.2(2)	1.25(19)	1.4(2)	0.49(15)	0

[a] Wyckoff positions in *Cmcm* (No. 63): La1 and O1 in 4*c*; La2, Ni, and O2 in 8*g*; O3 and O4 in 8*e*.

[b] Empirically calculated atomic valence (16).

The *Amam* structure (Table 1) was re-refined using low-temperature neutron powder diffraction data collected on SEPD, in order to search for a low-temperature structural transition equivalent to the T_1 transition found in La_2NiO_4 (2). Temperature-dependent variations of Ni–O bond lengths, NiO_6 octahedral tilt angles, and Ni–O–Ni angles were sought. No such trends of any statistical significance were found, as the *Amam* model fitted 20 K equally as well as 300 K data. Lattice parameters are presented as a function of temperature in Fig. 5, showing no evidence of a low-temperature tetragonal ($a = b \approx 5.5$ Å) phase transition. Plots of Ni–O bond lengths and angles as a function of temperature (not shown) display monotonic dependence mimicking that of the lattice parameter versus temperature plots. Similarly, high *d*-spacing neutron powder diffraction data at low temperatures showed no evidence for magnetic ordering equivalent to the AF magnetic structure of La_2NiO_4 (1), nor was any evidence seen for charge ordering (5).

Structure of $La_3Ni_2O_{7.05}$

The structure of $La_3Ni_2O_{7.05}$ was refined from 300 K SEPD data, using the *Amam* structure of $La_3Ni_2O_{7.02}$ as a starting model. The results of the refinement are presented in Table 3, and the final fit to observed data in Fig. 6*a*. Fractional occupancies of oxygen atom sites remained close to 100% and were not included in the final refinement. The 0.7% oxygen excess based on titration results was not modeled. There are no significant differences with the final refined structure of $La_3Ni_2O_{7.02}$, despite the significant differences in resistivity between the two samples (Fig. 2). Also as for $La_3Ni_2O_{7.02}$, re-refinement of the structure using low-temperature SEPD data revealed no evidence for further symmetry lowering or magnetic/charge ordering.

Structure of $La_4Ni_3O_{10.03}$

The structure of $La_4Ni_3O_{10.03}$ was refined from 300 K SEPD data, starting from the *Fmmm* model of Zhang *et al.* (6), which gave a reasonable fit to observed data. As for the $n = 2$ phase, however, a number of unindexed peaks remained which could not be accounted for by a small NiO impurity. Introducing an NiO_6 octahedral rotational mode about *a* and retaining *c* as the long axis gives a resultant space-group symmetry *Bmab*, with allowed reflections at the *d*-spacings of peaks unfitted in *Fmmm*. Refining positional and isotropic displacement parameters in *Bmab*, after

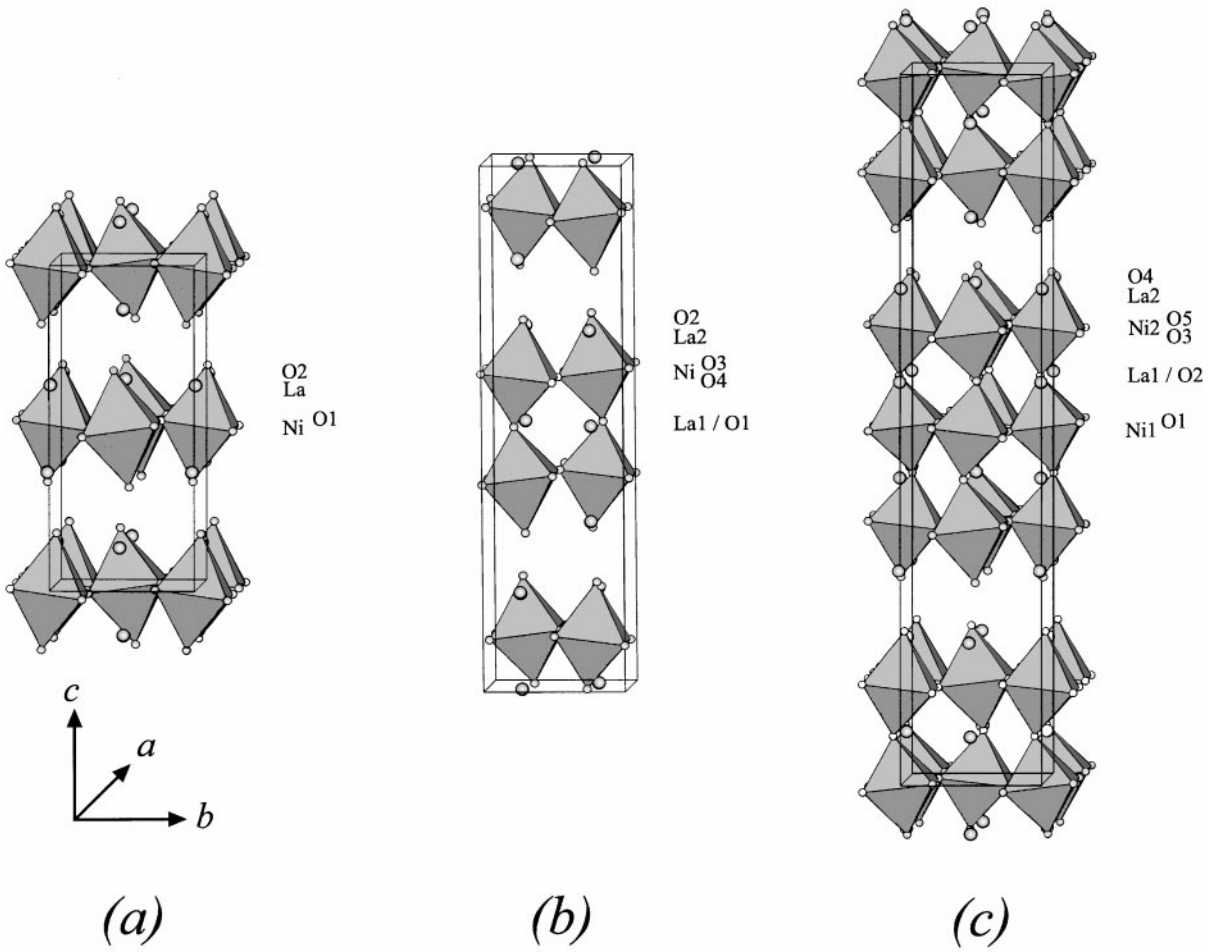

FIG. 3. (*a*) The structure of La_2NiO_4 refined at 250 K (2) compared to the final Rietveld-refined structures of (*b*) $La_3Ni_2O_{7.02}$ and (*c*) $La_4Ni_3O_{10.03}$ at 300 K. All are viewed close to (1 0 0). NiO_6 octahedra are drawn, and lanthanum atoms are larger than oxygen atoms. The NiO_6 octahedral rotation mode about *a*, responsible for the lowering of symmetry from *Fmmm*, is readily apparent.

a small initial displacement of oxygen atoms, resulted in a satisfactory fit to observed data. Refined anisotropic displacement parameters on oxygen atom sites were found to be reasonable. Fractional occupancies of oxygen atom sites remained close to 100% and were not included in the final refinement. The 0.3% oxygen excess based on titration results was not modeled. Details of the final refined structure of $La_4Ni_3O_{10.03}$ are presented in Table 4, the final fit to observed data is shown in Fig. 6*b* and the structure is shown in Fig. 3*c*.

This final refined *Bmab* structure is essentially the same as the *Cmca* structure published by Tkalich *et al.* (8). The greater precision of the data available in the present study does, however, suggest some more subtle features of the structure. In particular, the refined anisotropic displacement parameter of O1 was much larger than for any other atom, with the majority of the displacement residing perpendicular to the Ni1–O1 bond (Fig. 7*b*). The orientation of this anisotropy was even more pronounced when the structure was re-refined using low-temperature SEPD data.

As in the case of the $n = 2$ phase, analysis of the structure with low-temperature SEPD data revealed no evidence for a further low-temperature phase transformation. The *Bmab* structure fitted 20 K data equally as well as 300 K data, and, as noted by Tkalich *et al.* (8), there was no indication of the structure being tetragonal at low temperatures. There was likewise no evidence for magnetic ordering at low temperatures in high *d*-spacing neutron powder diffraction data.

IV. DISCUSSION

The most obvious result obtained in the above refinements is the symmetry lowering of $La_3Ni_2O_7$ from *Fmmm* to *Amam* in both the air-annealed and oxygen-annealed

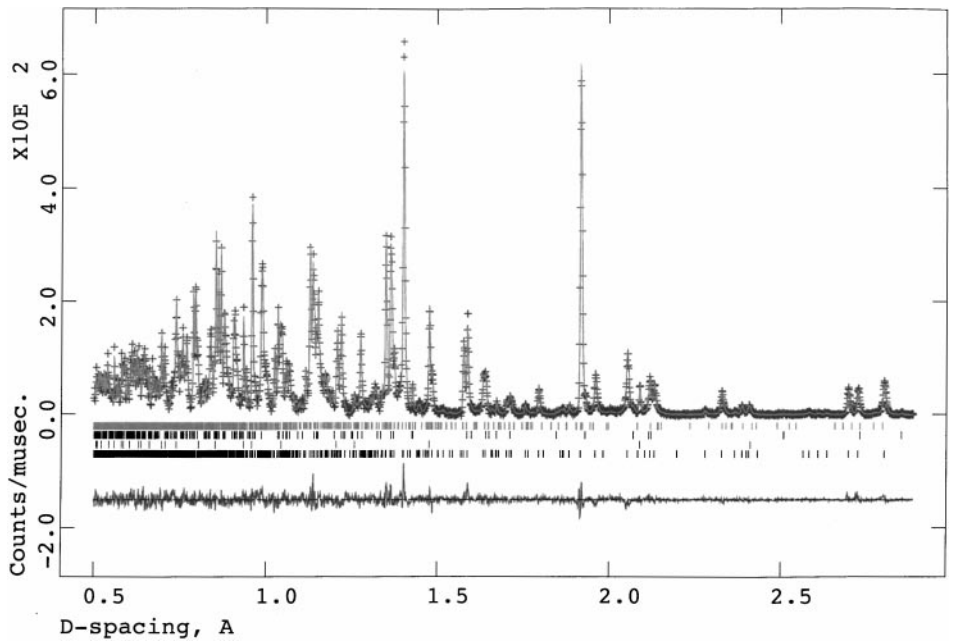

FIG. 4. Final observed (+), calculated, and difference (below) neutron powder diffraction profiles for $La_3Ni_2O_{7.02}$. The top row of reflection markers refers to 6.7(3) wt % $La_4Ni_3O_{10}$, the second row to 3.42(11) wt % La_2NiO_4, and the third row to 1.80(3) wt % NiO. Data were collected on backscattering detector bank of GPPD at 300 K.

samples. The quality of the refinements, and the clear structural relationship of this $n = 2$ RP phase to the *Bmab* structures of its $n = 1$ and 3 homologues, give credibility to this structure.

The apical oxygen O2 of the NiO_6 octahedron that projects into the NaCl-type layer (Fig. 1*b*), is by far the most problematic oxygen site in the refined structure of $La_3Ni_2O_{7.02}$. Its calculated atomic valence (1.707) is furthest from the expected value of 2, and its long bond to Ni (2.232(5) Å) distorts the otherwise quite regular NiO_6 octahedron. This does not, however, appear to be a unique feature of the $n = 2$ phase. Table 5 compares equivalent octahedral tilt angles and bond lengths among $n = 1$, 2, and 3 RP phases $La_{n+1}Ni_nO_{3n+1}$. The elongation of the Ni–O bond projecting into the NaCl-type layer is common to all these phases. The low calculated atomic valence at that oxygen site is also found across the series. Both features reflect the fact that this is the only oxygen site contributing to both perovskite-type and NaCl-type structural units in these RP phases, and is therefore subject to competing crystal-chemical driving forces.

TABLE 2
Space Group Comparison for $La_3Ni_2O_{7.02}$ from GPPD Neutron Powder Data at 300 K

	Fmmm	*Amam*	Valence[a]	*Fmmm*	*Amam*
Ni–O1 (Å)	1.946(5)	1.9377(19)	La1	2.596	2.750
Ni–O2 (Å)	2.204(14)	2.232(5)	La2	2.327	2.817
Ni–O3 (Å)	1.91501(19)	1.908(2)	Ni	2.638	2.562
Ni–O4 (Å)	—	1.940(2)	O1	1.807	1.841
R_p	0.1191	0.0453	O2	1.665	1.707
R_{wp}	0.1639	0.0634	O3	2.071	2.106
$R(F^2)$	0.1430	0.0398	O4	—	2.020
χ^2	11.32	1.700			

[a] Empirically calculated atomic valence (16).

It can be seen from Table 5 that the nature of the NiO_6 octahedral rotation mode is essentially the same for the $n = 1$, 2, and 3 RP phases. Ni–O–Ni angles in the xy plane are approximately 170 °, with the only significant distortion of the octahedra being the elongated apical bond into the NaCl-type layer. The $n = 3$ phase is the lowest order of n in which an NiO_6 octahedron (about Ni1) is completely isolated from the NaCl-type layer, and therefore is not elongated. It appears to be a relatively strained octahedron, as manifest in the large anisotropic displacement parameters of O1 perpendicular to the Ni1–O1 bond (Fig. 7*b*). This is a consequence of the increasingly perovskite-like character of the RP series with increasing n. The $n = \infty$ (i.e., perovskite-type) phase $LaNiO_3$ at room temperature and below has a tetragonal $R\bar{3}c$ structure in which perfectly regular NiO_6 octahedra rotate via a quite different mode from ideal perovskite-type (17). At the Ni1 site in $La_4Ni_3O_{10}$, the crystal-chemical driving forces responsible for the $R\bar{3}c$ structure of $LaNiO_3$ are felt more strongly than at the Ni2

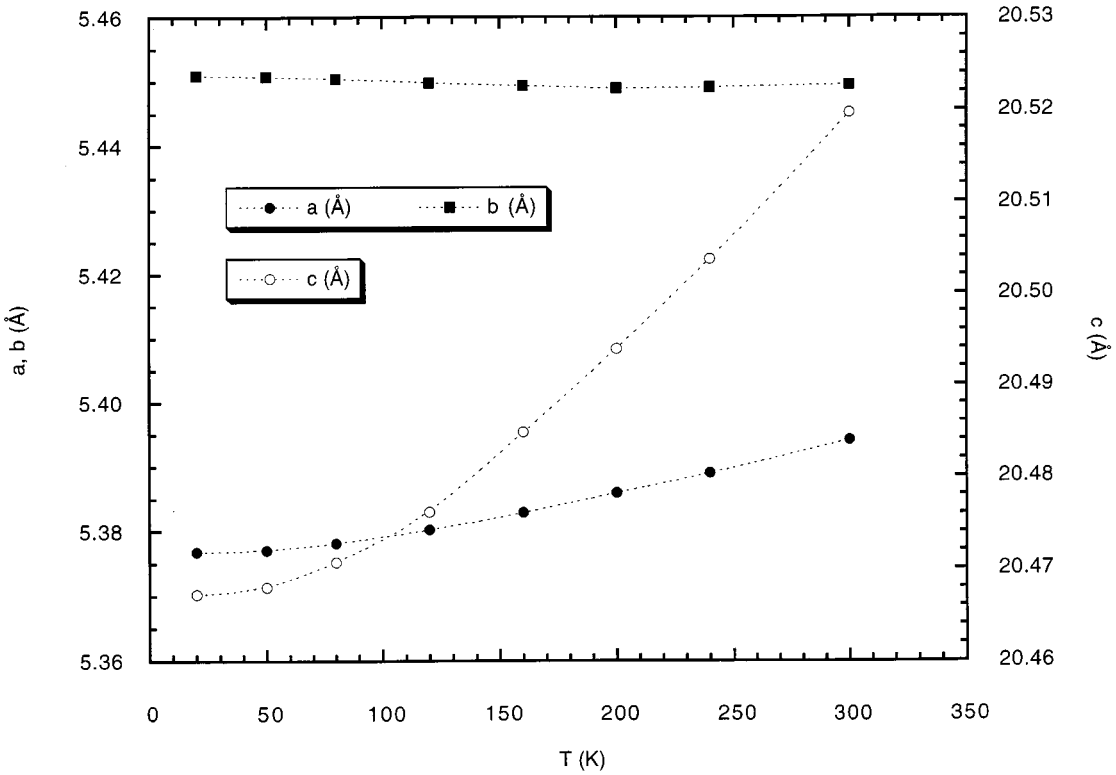

FIG. 5. Temperature dependence of the lattice parameters of $La_3Ni_2O_{7.02}$. Error bars are smaller than symbols.

site, or at the Ni sites in $La_3Ni_2O_7$ and La_2NiO_4. The resulting strain within the perovskite-type blocks clearly increases with n, hence the synthetic difficulties associated with the higher-order RP phases.

Further evidence of the increasingly perovskite-like environment occupied by $Ni1O_6$ octahedra when $n = 3$ is found in the empirically calculated bond valence sums (16). The calculated bond valence for Ni1 when $n = 2$ is 2.56 (Tables 2 and 3), close to the expected value of 2.50. For $n = 3$, the expected values for both Ni sites is 2.67, but the calculated values are 2.83 (Ni1) and 2.60 (Ni2) (Table 4). This apparent charge disproportionation suggests a preference for Ni^{3+} to occupy the Ni1 site and for Ni^{2+} to occupy the Ni2 site. This is consistent with the perovskite-like environment of the $Ni1O_6$ octahedra (all Ni are 3+ in $LaNiO_3$ perovskite) and the $n = 2$-like environment of the $Ni2O_6$ octahedra (average Ni valence is 2.50 in $n = 2$ $La_3Ni_2O_7$). It should be noted that when the $n = 3$ sample was cooled to 20 K, the extent of this charge disproportionation was unaffected.

TABLE 3
Crystal Structure Data for $La_3Ni_2O_{7.05}$ from SEPD Neutron Powder Data at 300 K

Amam (*Cmcm*)[a]: $a = 5.39710(19)$, $b = 5.45011(19)$, $c = 20.5074(10)$ Å
$R_p = 0.0543$, $wR_p = 0.0825$, $R(F^2) = 0.0456$, $\chi^2 = 4.842$

	x (a)	y (b)	z (c)	$100U_{iso}$ (Å^2)	Valence[b]
La1	$\frac{1}{4}$	0.2486(18)	$\frac{1}{2}$	0.77(9)	2.809
La2	$\frac{1}{4}$	0.2545(10)	0.31812(12)	0.43(5)	2.831
Ni	$\frac{1}{4}$	0.2538(10)	0.09506(12)	0.36(5)	2.560
O1	$\frac{1}{4}$	0.2931(16)	0	1.57(18)	1.891
O2	$\frac{1}{4}$	0.2173(12)	0.2039(3)	1.72(11)	1.717
O3	0	$\frac{1}{2}$	0.1053(2)	0.79(9)	2.163
O4	$\frac{1}{2}$	0	0.0884(2)	0.85(10)	1.971

[a] Wyckoff positions in *Cmcm* (No. 63): La1 and O1 in 4*c*; La2, Ni, and O2 in 8*g*; O3 and O4 in 8*e*.
[b] Empirically calculated atomic valence (16).

The presence of a low-temperature phase transition in La_2NiO_4 (2), and its absence in $La_3Ni_2O_7$ and $La_4Ni_3O_{10}$, is presumably related to this stress within the perovskite-type layer as n increases. In the low-temperature $P4_2/ncm$ phase of La_2NiO_4, NiO_6 octahedra rotate about the (1 1 0) direction, as opposed to the (1 0 0) direction in the *Bmab* phase. The (1 1 0) rotational mode has no greater similarity to the modes found in $LaNiO_3$ than does the (1 0 0) rotational mode, therefore the low-temperature transition is a consequence of subtle interactions between the perovskite-type and NaCl-type layers, not within the perovskite-type layer itself. The presence of additional strain from

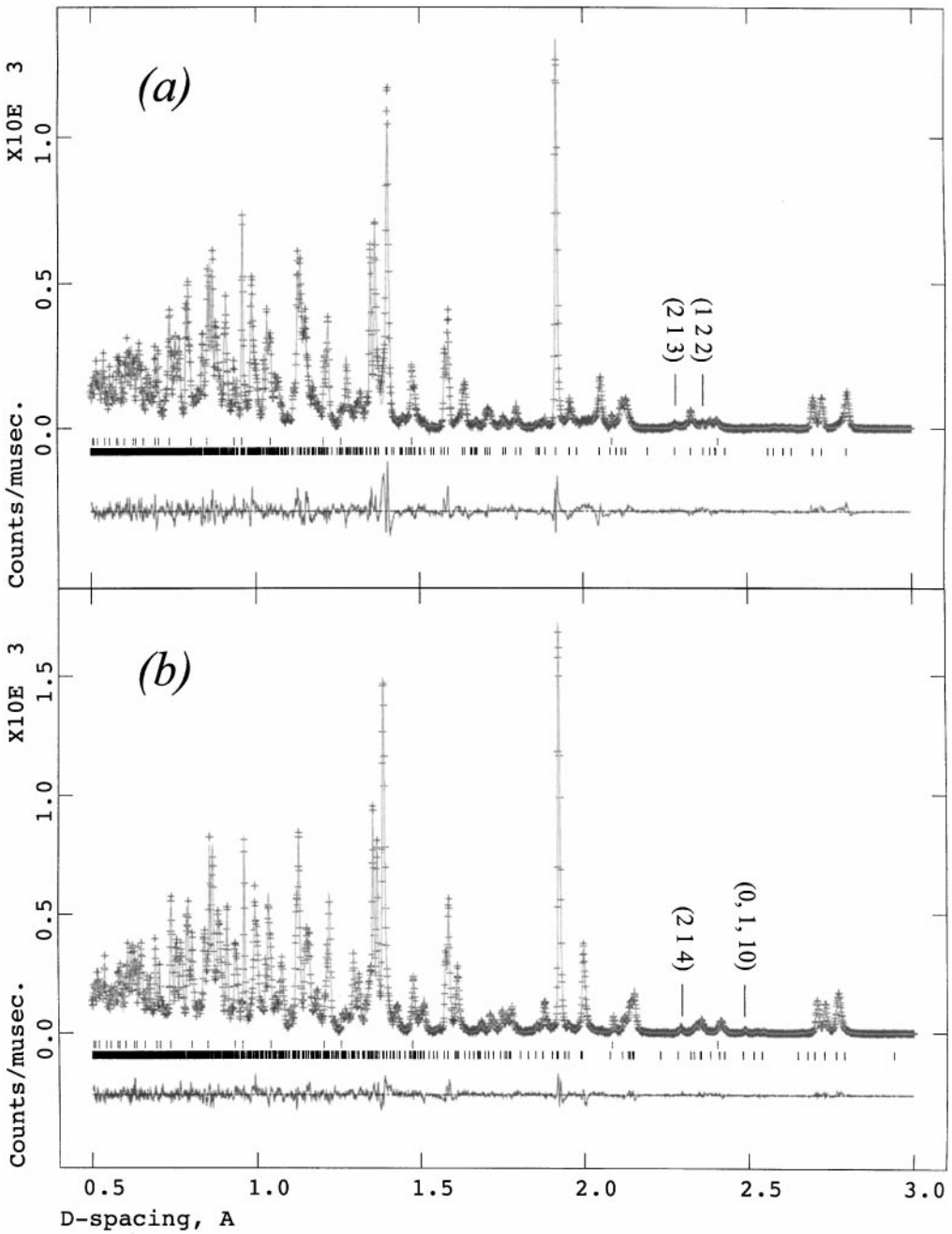

FIG. 6. Final observed (+), calculated, and difference (below) neutron powder diffraction profiles for (*a*) $La_3Ni_2O_{7.05}$ and (*b*) $La_4Ni_3O_{10.03}$. The top row of reflection markers refers to NiO, 0.64(3) wt % in (*a*) and 1.08(2) wt % in (*b*). Data were collected on backscattering detector bank of SEPD at 300 K. Some prominent reflections forbidden in *Fmmm* are marked.

within the perovskite-type layer appears to make the low-temperature phase untenable for $n > 1$.

Evidence of magnetic ordering, such as the AF ordering which occurs for the $n = 1$ phase (2), was not observed in neutron diffraction data for the $n = 2$ or $n = 3$ phases, despite low-temperature anomalies in the resistivity curves of both compounds (Fig. 2). These phases therefore do not appear to support either long-range magnetic order or long-range charge order, with the exception of some possible charge disproportionation between the Ni1 and Ni2 sites when $n = 3$. Short-range charge-ordered regions, or charge-density waves, do, however, remain as a possible

TABLE 4
Crystal Structure Data for $La_4Ni_3O_{10.03}$ from SEPD Neutron Powder Data at 300 K

Bmab (*Cmca*)[a]: $a = 5.41327(11)$, $b = 5.46233(11)$, $c = 27.9605(7)$ Å
$R_p = 0.0363$, $wR_p = 0.0532$, $R(F^2) = 0.0323$, $\chi^2 = 2.417$

	x (a)	y (b)	z (c)	$100U_{iso}$ (Å^2)	Valence[b]
La1	0	−0.0015(10)	0.43263(12)	0.76(5)	2.822
La2	0	−0.0092(10)	0.30032(8)	0.42(5)	2.882
Ni1	0	0	0	0.33(6)	2.825
Ni2	0	−0.0037(8)	0.13805(7)	0.37(4)	2.599
O1	$\frac{1}{4}$	$\frac{1}{4}$	0.0057(3)	—	1.975
O2	0	0.9553(7)	0.06893(18)	—	1.909
O3	$\frac{1}{4}$	$\frac{1}{4}$	0.1338(2)	—	2.004
O4	0	0.0301(13)	0.21469(16)	—	1.7074
O5	$\frac{1}{4}$	$\frac{3}{4}$	0.1451(2)	—	2.120
	U_{11}	U_{22}	U_{33}	U_{12}	U_{23}
O1	3.2(3)	3.0(3)	0.6(4)	−2.22(19)	0
O2	0.37(16)	1.0(1)	1.49(16)	0	0.1(2)
O3	0.2(2)	1.0(3)	1.8(3)	−0.33(16)	0
O4	2.2(3)	1.7(3)	0.70(16)	0	−0.9(2)
O5	1.3(3)	0.7(2)	1.5(3)	0.58(16)	0

[a] Wyckoff positions in *Cmca* (No. 64): La1, La2, Ni2, O2, and O4 in 8*m*; Ni1 in 4*a*; O1, O3, and O5 in 8*e*.
[b] Empirically calculated atomic valence (16).

TABLE 5
Equivalent NiO_6 Octahedra in $La_{n+1}Ni_nO_{3n+1}$ ($n = 1, 2, 3$)

La_2NiO_4[a]		$La_3Ni_2O_{7.02}$[b]		$La_4Ni_3O_{10.03}$[c]	
Angles (deg)	bonds (Å)	Angles (deg)	bonds (Å)	Angles (deg)	bonds (Å)
Ni–O1–Ni	173.0(2)	—	—	Ni1–O1–Ni1	170.2(5)
Ni–O1	1.9442(2)	—	—	Ni1–O1	1.9297(7)
—	—	—	—	Ni1–O2	1.950(5)
—	—	Ni–O4–Ni	171.0(2)	Ni2–O3–Ni2	172.8(3)
—	—	Ni–O3–Ni	169.0(2)	Ni2–O5–Ni2	168.5(4)
—	—	Ni–O4	1.940(2)	Ni2–O3	1.943(3)
—	—	Ni–O3	1.908(2)	Ni2–O5	1.916(3)
Ni–O2	2.235(2)	Ni–O2	2.232(5)	Ni2–O4	2.170(5)
—	—	Ni–O1	1.9733(19)	Ni2–O2	1.950(5)

[a] Rodriguez-Carvajal *et al.* (2), data collected at 250 K.
[b] Present study, data collected on GPPD at 300 K.
[c] Present study, data collected on SEPD at 300 K.

explanation for observed resistivity anomalies; the powder neutron diffraction data used in the present study is not sufficiently sensitive to the diffuse intensity which would be associated with such features. Single-crystal neutron diffraction and high-resolution (synchrotron) XRD studies will be necessary to finally determine whether any subtle charge ordering is occurring at low temperatures.

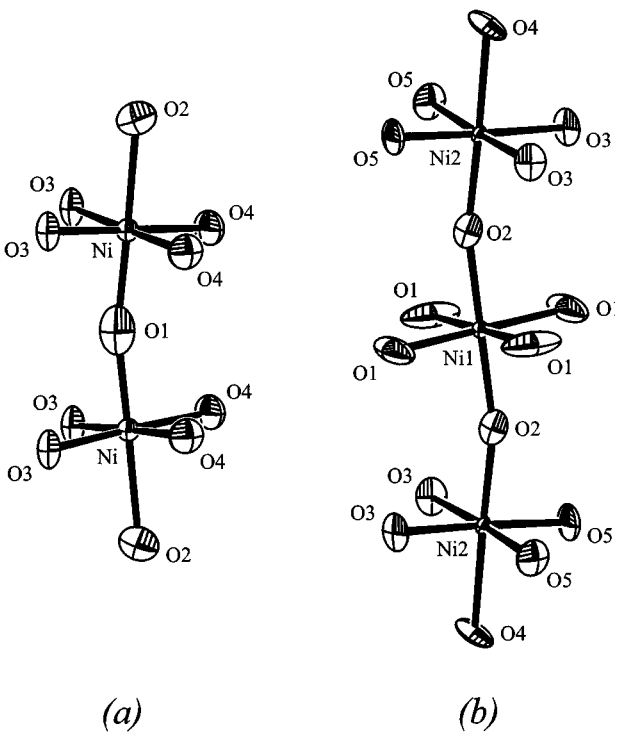

FIG. 7. ORTEP plots (95% probability) of NiO_6 octahedra in the perovskite-type layers of (*a*) $La_4Ni_3O_{7.02}$ and (*b*) $La_4Ni_3O_{10.03}$ at 300 K. Note that only oxygen sites have been refined anisotropically.

ACKNOWLEDGMENTS

This work was supported by the U.S. Department of Energy, Basic Energy Sciences—Materials Sciences, under Contract W-31-109-ENG-38 (C.D.L., D.N.A.).

REFERENCES

1. G. Aepelli and D. J. Buttrey, *Phys. Rev. Lett.* **61,** 203 (1988).
2. J. Rodríguez-Carvajal, M. T. Fernández-Díaz, and J. L. Martínez, *J. Phys.: Condens. Matter* **3,** 3215 (1991).
3. D. J. Buttrey, P. Ganguly, J. M. Honig, C. N. R. Rao, R. R. Schartman, and G. N. Subbanna, *J. Solid State Chem.* **74,** 233 (1988).
4. Z. Zhang, M. Greenblatt, and J. B. Goodenough, *J. Solid State Chem.* **108,** 402 (1994).
5. S. Tanaguchi, T. Nishikawa, Y. Yasui, Y. Kobayashi, J. Takeda, S. Shamoto, and M. Sato, *J. Phys. Soc. Jpn.* **65,** 1644 (1995).
6. Z. Zhang and M. Greenblatt, *J. Solid State Chem.* **117,** 236 (1995).
7. P. H. Lacorre, *J. Solid State Chem.* **97,** 495 (1992).
8. A. K. Tkalich, V. P. Glazkov, V. A. Somenkov, S. S. Shilshtein, A. E. Kar'lin, and A. V. Mirmel'shtein, *Superconductivity* **4,** 2281 (1992).
9. A. C. Larson and R. B. V. Dreele, "GSAS: The General Structure Analysis System." Los Alamos National Laboratory, Los Alamos, NM, 1991.
10. K. Sreedhar, M. McElfresh, D. Perry, D. Kim, P. Metcalf, and J. M. Honig, *J. Solid State Chem.* **110,** 208 (1994).
11. R. J. Cava, B. Batlogg, T. T. Palstra, J. J. Krajewski, J. W. F. Peck, A. P. Ramirez, and J. L. W. Rupp, *Phys. Rev. B* **43,** 1229 (1991).
12. K. Sreedhar, J. M. Honig, M. Darwin, M. McElfresh, P. M. Shand, J. Xu, B. C. Crooker, and J. Spalek, *Phys. Rev. B* **46,** 6382 (1992).
13. D. C. Johnston, *Phys. Rev. Lett.* **62,** 959 (1989) and references therein.
14. E. Dagatto and T. M. Rice, *Science* **271,** 618 (1996).
15. G. Wu and J. J. Neumeier, in preparation.
16. N. E. Brese and M. O'Keeffe, *Acta Crystallogr. B* **47,** 192 (1991).
17. J. L. García-Muñoz, J. Rodríguez-Carvajal, P. Lacorre, and J. B. Torrance, *Phys. Rev. B* **46,** 4414 (1992).